Draft version August 13, 2017
Typeset using LaTeX **twocolumn** style in AASTeX61

WATER, HIGH-ALTITUDE CONDENSATES, AND METHANE DEPLETION IN THE ATMOSPHERE OF THE WARM NEPTUNE WASP-107b

Laura Kreidberg[1, 2]

Michael Line[3]

Daniel Thorngren[4]

Caroline Morley[5, *]

Kevin Stevenson[6]

[1] *Harvard Society of Fellows 78 Mt. Auburn St.*
Cambridge, MA 02138, USA
[2] *Harvard-Smithsonian Center for Astrophysics 60 Garden St.*
Cambridge, MA 02138
[3] *Arizona State University*
[4] *University of California Santa Cruz*
[5] *Harvard-Smithsonian Center for Astrophysics*
[6] *Space Telescope Science Institute*

Submitted to ApJL

ABSTRACT

Keywords: planets and satellites: individual (WASP-107b), planets and satellites: atmospheres

Corresponding author: Laura Kreidberg
laura.kreidberg@cfa.harvard.edu

* Sagan Fellow

1. INTRODUCTION

The composition of a planet's atmosphere depends on where and how the planet formed. By measuring atmospheric metallicity and molecular abundance ratios, we can shed light on important aspects of the formation process such as location within the disk and the relative accretion rates of gas versus solids (Öberg et al. 2011; Fortney et al. 2013; Madhusudhan et al. 2014; Ali-Dib 2016; Mordasini et al. 2016; Espinoza et al. 2017).

The warm Neptune WASP-107b is an intriguing target for atmosphere characterization for several reasons. It is an intermediate size between ice giants and gas giants, with a mass similar to Neptune's and a radius close to Jupiter's ($0.12\,M_{\mathrm{Jup}}$, $0.94\,R_{\mathrm{Jup}}$; Anderson et al. 2017). Studying the atmospheres of planets in this transition region will provide additional clues in the much-debated mystery of what stunts the growth of Neptune-size planets (e.g Pollack et al. 1996; Dawson et al. 2016; Frelikh & Murray-Clay 2017).

WASP-107b also has a relatively low equilibrium temperature (780 K) compared to most other exoplanets that are amenable to atmosphere characterization. This results in a distinct atmospheric chemistry from other well-studied systems: at low temperatures, the dominant molecular reservoir for carbon transitions from carbon monoxide to methane (Moses et al. 2013). Spectral features from both water and methane are accessible with current observing facilities, raising the possibility of a spectroscopic estimate of the carbon-to-oxygen ratio (C/O). Previous measurements of C/O have been challenging because they rely on photometry that covers absorption features from multiple molecules (e.g. Madhusudhan et al. 2011; Line et al. 2014; Benneke 2015; Kreidberg et al. 2015). FIXME: maybe cut this.

In addition, WASP-107b is one of the best targets discovered to date for atmosphere characterization. Thanks to its large atmospheric scale height and small, bright host star, the expected signal-to-noise for the transmission spectrum is comparable to the best studied benchmarks in the field (e.g. HD 209458b, HD 189733b). The planet is also a feasible target for thermal emission measurements, with an expected secondary eclipse depth of $\sim 0.1\%$ in *Spitzer*'s $4.5\,\mu$m channel. In this paper we report the first atmosphere characterization of WASP-107b: a near-infrared transmission spectrum measured with the *Hubble Space Telescope* (*HST*).

2. OBSERVATIONS

We observed a single transit of WASP-107b with HST's Wide Field Camera 3 (WFC3) instrument on UT 5-6 June 2017. The transit observation consisted of five HST orbits. At the beginning of each 96-minute orbit, we took an image of the target with the F130N filter (exposure time = 4.2 s). This direct image is used for wavelength calibration. For the remainder of the target visibility period (about 45 minutes), we obtained time series spectra with the G141 grism, which provides low-resolution spectroscopy over the wavelength range $1.1-1.7\,\mu$m. We used the NSAMP=6, SPARS_25 readout mode (exposure time = 112 s) to optimize the efficiency of the observations, as determined by the `PandExo_HST` planning tool[1]. As is standard for WFC3 observations of bright targets, we used the spatial scanning observing mode, which slews the telescope in the spatial direction over the course of an exposure. The scan rate was 0.12 arcseconds/sec.

3. DATA REDUCTION

We reduced the data with the custom pipeline described in Kreidberg et al. (2014), which we summarize briefly here. For each exposure, we extracted the spectrum from each up-the-ramp sample (or "stripe") separately using the optimal extraction algorithm of Horne (1986). The stripe spectra were then summed to create the final spectrum. For each stripe, the extraction box was 80 pixels high and centered on the stripe's midpoint in the spatial direction. To correct the change in dispersion solution over the length of the spatial scan, we interpolated each row to the wavelength scale of the row corresponding to the spectral trace. We then corrected for slight drift in the spectral direction (< 0.1 pixels) by interpolating each spectrum to the wavelength scale of the first exposure. To subtract the background, we took the median of sky pixels that were uncontaminated by the target spectrum (rows $5-250$, columns $5-15$). The typical background counts were low: 40 photoelectrons/pixel, in comparison to 3×10^4 photoelectrons/pixel in the stellar spectrum.

4. LIGHT CURVE ANALYSIS

The data analysis had two parts: the band-integrated "white" light curve fit and the spectroscopic light curve fits.

4.1. *White Light Curve*

To create the raw white light curve, we summed each spectrum over the 181 pixels in the spectral trace. The white light curve has systematic trends that are typical for WFC3 observations (Zhou et al. 2017): the flux increases increases asymptotically over each orbit (the "ramp" effect) and there is a visit-long linear

[1] https://github.com/spacetelescope/PandExo_HST

trend. The largest ramp occurs in the initial orbit (orbit zero), so we only fit data from orbits one through four in our analysis, following common practice. We fit the light curve with the analytic model of the form $F_{\rm white}(t) = S_{\rm white}(t) \times T_{\rm white}(t)$, where $S_{\rm white}$ is a systematics model and $T_{\rm white}$ is a transit model. We used the same systematics model as Kreidberg et al. (2015), Equation 1. To model the transit, we used the `batman` package (Kreidberg 2015). The transit model parameters are the orbital period p, time of inferior conjunction t_0, transit depth r_p/r_s, ratio of semi-major axis to stellar radius a/r_s, orbital inclination i, and the quadratic stellar limb darkening parameters u_1 and u_2.

4.1.1. *Star Spot Crossing*

In our initial analysis, we noticed a bump in the light curve during orbit three that was not fit well with our model. We attribute this feature to a star spot crossing event, as WASP-107 is an active star and spot crossings have been observed before (Dai & Winn 2017; Močnik et al. 2017). In our subsequent analysis, we gave the data in orbit three no weight in the fit. The amplitude of the spot crossing feature is 300 ppm, as illustrated in Figure 1.

4.1.2. *Final Fit*

In our final fit, we fixed the transit parameters a/r_s, i, p on the precise estimates from the Kepler light curve (Dai & Winn 2017). These values are consistent with our best fit when we allowed them to vary freely. We also fixed the limb darkening parameters on predictions from a PHOENIX model for a star with effective temperature 4300 K, calculated with the `limb-darkening` package from Espinoza & Jordán (2015). The remaining free parameters were t_0, r_p/r_s, and the systematics parameters for the visit-long and orbit-long trends.

For the best fit white light curve, the root-mean-square (rms) residuals were 93 ppm (excluding the star spot crossing), which is somewhat larger than the expected shot noise of 50 ppm. We attribute the excess noise to loss of flux off the edge of the detector, which can occur if there is variation in the position or length of the spatial scan. There is no evidence for correlated noise in the residuals, so to account for the excess noise we simply increased the per-point uncertainties by a factor of 1.7 to achieve a χ^2_ν value of unity. We then used the Markov chain Monte Carlo (MCMC) algorithm to estimate parameter uncertainties (Foreman-Mackey et al. 2013). The chain had 50 walkers which each ran for 10^4 steps with the first 10% discarded as burn-in. We tested for convergence by dividing the chain in two halves and confirming that they gave consistent results. The transit time was $t_0 = 2457910.45407 \pm 6{\rm e}{-5}$ $\rm BJD_{TDB}$ and the planet/star radius was $r_p/r_s = 0.14399 \pm 0.00017$.

4.2. *Spectroscopic Light Curve Fits*

We binned the spectrum into 20 spectrophotometric channels from 1.12 to 1.65 μm, shown in Figure 1. We fit the light curves with the `divide-white` technique, which assumes that the light curve systematics have the same morphology at all wavelengths (Stevenson et al. 2014; Kreidberg et al. 2014). For this method, the transit model $T_\lambda(t)$ is multiplied by the systematics vector from the white light curve fit ($F_{\rm white}/T_{\rm white}$), and rescaled by a factor $C_\lambda + V_\lambda t$. One advantage of this approach is that it removes the star spot crossing feature, enabling us to use orbit three with no additional correction. The amplitude of the feature has no detectable wavelength dependence at the level of precision of our data. As for the white light curve, we fixed some of the transit parameters on the estimates from Dai & Winn (2017) and fixed the limb darkening on the PHOENIX model. The final spectroscopic light curve fits had just three free parameters: C_λ, V_λ, and r_p/r_s.

The best fit light curves have a median χ^2_ν value of 1.16. To ensure that we did not underestimate the uncertainty on the transit depths, we rescaled the photometric uncertainties for all spectroscopic channels such that the χ^2_ν values are unity. We performed an MCMC fit to the light curves with `emcee`. For each light curve we ran a fit with 50 walkers and 1000 steps per walker, and tested for convergence as we did for the white light curve. The median transit depths and $1\,\sigma$ uncertainties are given in Table 1.

We explored several alternative choices for the spectroscopic light curve fits, but found that none of them made a significant difference in the transmission spectrum. For example, we fit the spectroscopic light curves with the same analytic model we used for the white light curve and obtained nearly identical relative transit depths (differing by just 0.3σ on average), except with a small constant offset due to the uncorrected star-spot crossing feature. This offset does not affect our final analysis because the planet's one-bar radius is a free parameter in the atmospheric retrieval (see § 5.2). We also fit for a linear limb darkening parameter rather than fixing the limb darkening on the PHOENIX model values. We found that the fitted limb darkening coefficients are consistent with the model predictions, so we opted to fix the coefficients in our final analysis because it improves the precision on the transit depths by about 10%. We also checked that the uncertainty in the stellar parameters does not significantly affect the PHOENIX model predictions at the level of precision of our data.

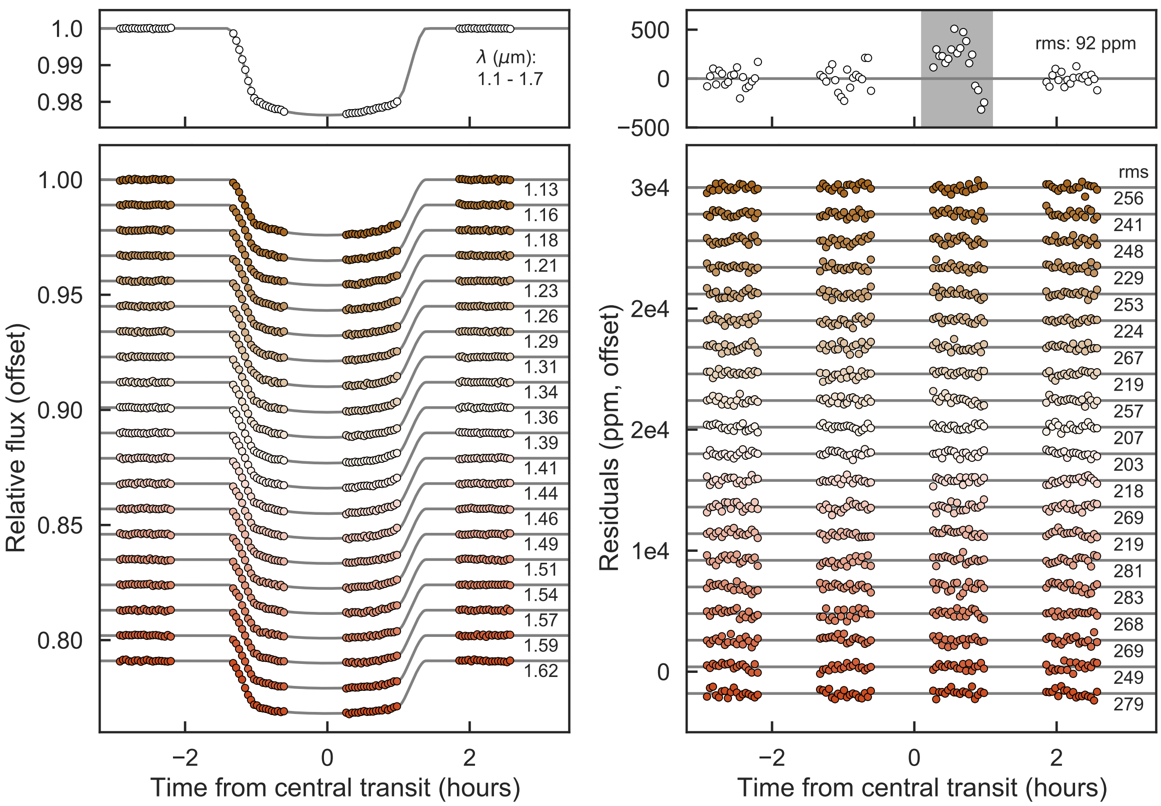

Figure 1. Broadband and spectrophotometric transit light curves for WASP-107b measured with *HST*/WFC3 compared to best fit models (left) and residuals from the best fit (right). Annotations indicate the central wavelength and root-mean-square (rms) residuals for each light curve. A possible star-spot crossing feature is shaded in gray in the upper right; our systematic error correction removes this feature from the spectroscopic light curves.

4.2.1. *Transit Depths Redder than 1.62 μm*

The red edge of the transmission spectrum is of interest for our analysis because methane is expected to be the dominant absorber over water at wavelengths greater than 1.6 μm. Unfortunately, we find that the our reddest spectroscopic light curves ($> 1.62\mu$m) are too poor in quality to robustly measure the transit depth. The residuals exhibit correlated noise and the fits have $\chi^2_\nu > 2$. The transit depths are also sensitive to which method we use to fit for instrument systematics. We therefore opt not to report transit depths redder than the 1.62 μm channel.

4.2.2. *Independent Analysis*

We also performed an independent data reduction and fit using K. Stevenson's pipeline.

5. COMPOSITION OF THE ATMOSPHERE

In this section we discuss constraints on the composition of WASP-107b's atmosphere based on interior structure modeling and atmospheric retrieval of the measured transmission spectrum.

5.1. *Atmospheric Metallicity from Interior Structure Modeling*

Given WASP-107b's unusually low density, we quantitatively explored the range of atmospheric metallicities that are consistent with the observed mass and radius using the structure evolution modeling of Thorngren et al. (2016). These models assume a thermally inert heavy-element core with a convective envelope of additively mixed H/He (Saumon et al. 1995) and heavy-element impurities. The heavy elements were a 50-50 rock-ice mix from ANEOS (**?**). We evolved the planets in time using the atmospheric models of Fortney et al. (2007). The results are sensitive to assumptions about the stellar age, which is uncertain (either 0.6 ± 0.2 to 8.3 ± 4.3 Gyr depending on model assumptions; Močnik et al. 2017). We therefore ran two models, with uniform age priors of either $0.2 - 1.0$ or $1.0 - 13.8$ Gyr. We used

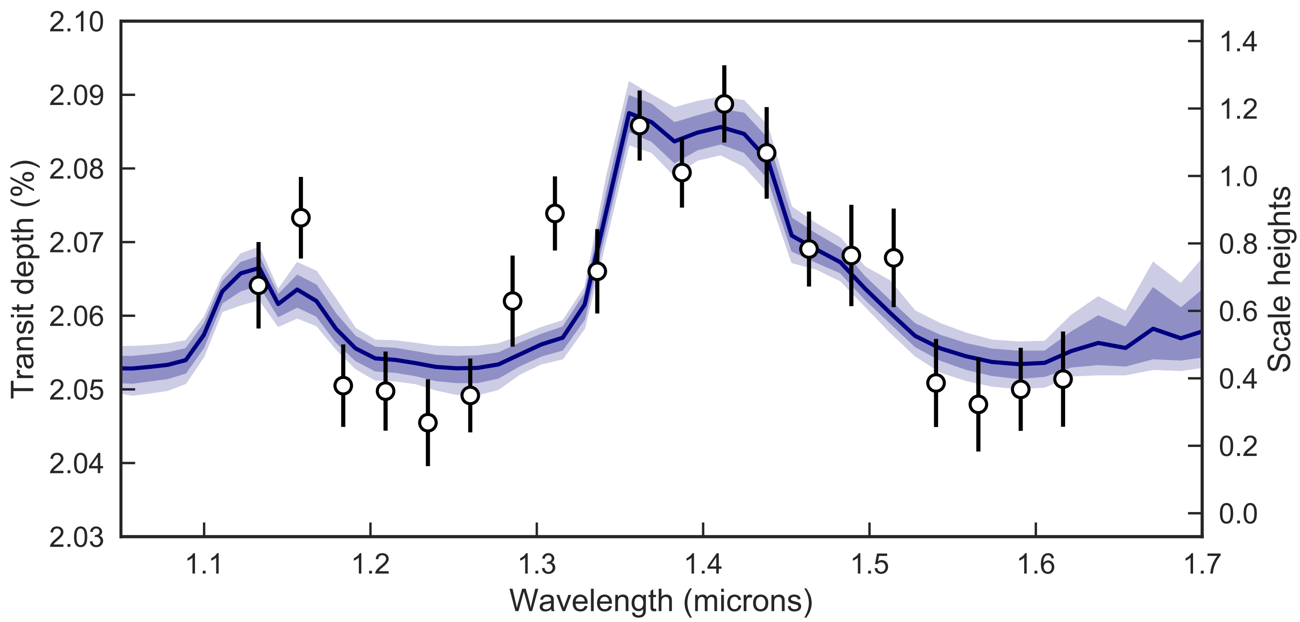

Figure 2. The transmission spectrum of WASP-107b (points with $1\,\sigma$ error bars) compared to retrieved models (blue line with shaded 1 and 2σ confidence intervals). The features at 1.15 and 1.4 μm are due to water absorption. The right-hand axis indicates the normalized atmospheric scale height assuming a $100\times$ solar composition.

the published mass and radius estimates ($0.12\pm0.01\ M_{\rm J}$, 0.94 ± 0.02; Anderson et al. 2017).

Based on these assumptions, we fit for envelope metallicity and core mass using an MCMC with uniform priors on both parameters. The MCMC burned in for 10^3 steps and then collected 4×10^6 samples, which we thinned to 10^5. The resulting envelope metal mass fractions were converted to metallicities by assuming the mean molecular weight of the metals was 18 (the value for water), using the approach of Fortney et al. (2013). Figure 3 shows the results. We find that the inferred atmospheric metallicity and core mass are inversely proportional, as expected (the more massive the core, the lighter the envelope must be to maintain the observed radius). Larger core masses and envelope metallicities are allowed for the younger stellar age since planets cool and contract as they age. For the younger (older) stellar age, we find an upper limit on the core mass of FIXME and an upper limit on atmospheric metallicity of FIXME.

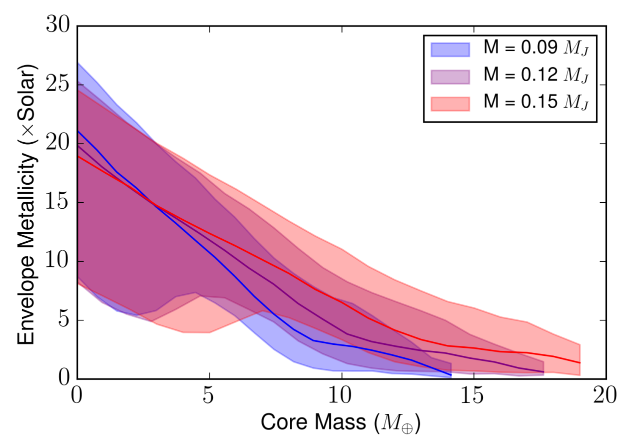

Figure 3. Estimated envelope metallicity and core mass based on interior structure modeling of the mass and radius of WASP-107b. FIXME ages.

5.2. *Retrieval*

We also inferred the composition of the atmosphere directly from the transmission spectrum using the CHIMERA chemically-consistent retrieval tool described in Kreidberg et al. (2015). Briefly, CHIMERA solves the transmission geometry problem using the equations in Brown (2001); Tinetti et al. (2012). We parameterize atmospheric composition with metallicity and carbon-to-oxygen ratio (C/O) under the assumption of thermochemical equilibrium using the NASA CEA routine (**?**) to compute the molecular abundances for H_2, He, H_2O, CH_4, CO, CO_2, NH_3, H_2S, Na, K, HCN, C_2H_2, TiO, VO, and FeH. We updated the transmission model to use correlated-K opacities (Lacis & Oinas 1991; Mollière et al. 2015; Amundsen et al. 2016) from the pre-tabulated line-by-line cross section database described in Freedman et al. (2014). The transmission forward model is coupled with the PyMultiNest tool

Table 1. WASP-107b transmission spectrum

Wavelength (μm)	Transit depth	Uncertainty
1.133	0.020641	5.9e-05
1.158	0.020733	5.5e-05
1.184	0.020505	5.6e-05
1.209	0.020498	5.4e-05
1.235	0.020455	5.9e-05
1.260	0.020492	5.0e-05
1.285	0.020620	6.2e-05
1.311	0.020739	5.0e-05
1.336	0.020660	5.7e-05
1.362	0.020858	4.8e-05
1.387	0.020794	4.8e-05
1.413	0.020888	5.2e-05
1.438	0.020821	6.2e-05
1.464	0.020691	5.1e-05
1.489	0.020682	6.9e-05
1.515	0.020679	6.7e-05
1.540	0.020509	6.0e-05
1.565	0.020480	6.4e-05
1.591	0.020500	5.6e-05
1.616	0.020514	6.5e-05

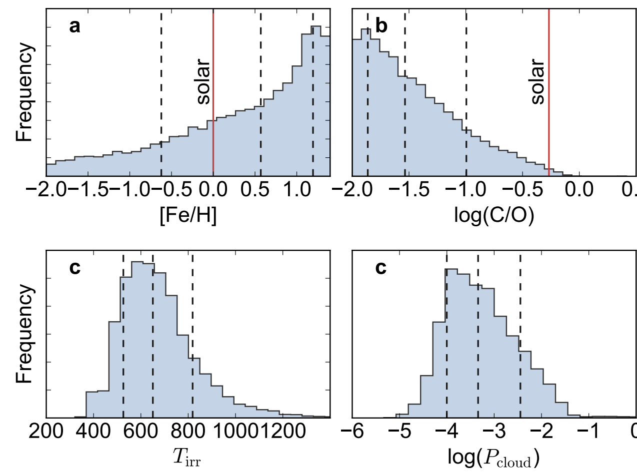

Figure 4. Retrieved distributions for (a) metallicity, (b) carbon-to-oxygen ratio, (c) irradiation temperature, and (d) cloud-top pressure. Dashed vertical lines show the median and $\pm 1\,\sigma$ confidence interval. Solar metallicity and C/O values are indicated with solid vertical lines.

(Buchner 2016) to solve the parameter estimation and model selection problems.

Our nominal model includes a temperature-pressure profile (parameterized via the Guillot 2010 relations), the atmospheric metallicity, the carbon-to-oxygen ratio, and a gray cloud-top pressure. We fix the T-P profile morphology but scale the irradiation temperature to allow for the unknown albedo and heat transport efficiency. We put a uniform prior on the atmospheric metallicity of $0.01 - 30\times$ solar based on the upper limit from § 5.1. Results are shown in Figure 4.

metallicity is degenerate with cloud-top pressure cloud at low pressures solar C/O is almost ruled out

and the quench pressures for nitrogen and carbon species (to account for transport-induced disequilibrium chemistry, e.g. Morley et al. 2017). for cloud patchiness (as described by Line et al. 2016).

We experiment with several scenarios within this framework, including models with/without clouds, models with/without quenching, including methane opacity, and a uniform prior in atmospheric metallicity from (FIXME to 30× solar based on the interior structure modeling). We also performed a "free" retrieval that allowed the abundances of CH_4, H_2O and NH_3 to vary freely.

We find strong evidence for water absorption (FIXME sigma) and clouds (FIXME sigma).

6. DISCUSSION

6.0.1. *Methane Abundance*

6.0.2. *Condensate Properties*

We also considered physically motivated, self-consistent cloud and haze models based on . To model WASP-107b's spectrum with self-consistent aerosols, we use the methods described in (Fortney et al. 2008; Morley et al. 2015). We include models from solar to 50× solar metallicity and solar C/O ratio. We model clouds that form in cool atmospheres (Na_2S, KCl, ZnS, see Morley et al. 2012), varying the cloud sedimentation efficiency from 0.1 to 3. None of the cloudy models are sufficiently low amplitude to match the observed muted signal. We also model an ad hoc photochemical 'soot' layer near the top of the atmosphere, scaling results from previous photochemical models for GJ 436b (Line et al. 2011; Morley et al. 2017). With a sufficiently thick photochemical haze with particle sizes around $0.03 - 0.1$ microns, the amplitude of the model water feature matches that of the observations.

7. DISCUSSION

We note that some directly imaged self-luminous planets in this temperature regime are also unexpectedly depleted in methane when compared to similar temperature brown dwarfs (Skemer et al. 2014). The leading hypothesis of this depletion (Zahnle & Marley 2014) is due to the CH4-CO quench point occurring in the CO stability field due to the low gravity of self-luminous planets when compared to brown dwarfs. In order this mechanism to work for neptune massed planet, the internal temperature would have to be near 500K to get the deep temperatures high enough to thermochemically deplete methane at the quench point. Given the age of the star, it is unlikely that such high internal temperatures are still due to heat of formation. It is possible that tidal heating could increase the internal temperature (Agundez et al. 2014; Morley et al. 2017) but that would require a negligible eccentricity, of which is currently uncertain for WASP107b.

7.1. *Comparative planetology with HAT-P-11b, HAT-P-26b*

8. CONCLUSIONS AND FUTURE PLANS

WASP-107b is slated to be observed with numerous facilities. Transits were recently observed with the WFC3/G102 grism and Spitzer 3.6 and 4.5 μm channels. Spitzer eclipses are planned (Program FIXME; PI L. Kreidberg). In addition, WASP-107b is included in the *JWST* Guaranteed Time Observations.

Combine data from Spitzer/HST JWST GTO

We thank Fei Dai, Jessica Spake, and Ian Crossfield for productive conversations. L.R.K. acknowledges support from the Harvard Society of Fellows and the Harvard Astronomy Department Institute for Theory and Computation.

Facilities: HST(WFC3)

REFERENCES

Ali-Dib, M. 2016, ArXiv e-prints, arXiv:1611.03128

Amundsen, D. S., Mayne, N. J., Baraffe, I., et al. 2016, A&A, 595, A36

Anderson, D. R., Collier Cameron, A., Delrez, L., et al. 2017, ArXiv e-prints, arXiv:1701.03776

Benneke, B. 2015, ArXiv e-prints, arXiv:1504.07655

Brown, T. M. 2001, ApJ, 553, 1006

Buchner, J. 2016, PyMultiNest: Python interface for MultiNest, Astrophysics Source Code Library, , , ascl:1606.005

Dai, F., & Winn, J. N. 2017, AJ, 153, 205

Dawson, R. I., Lee, E. J., & Chiang, E. 2016, ApJ, 822, 54

Espinoza, N., Fortney, J. J., Miguel, Y., Thorngren, D., & Murray-Clay, R. 2017, ApJL, 838, L9

Espinoza, N., & Jordán, A. 2015, MNRAS, 450, 1879

Foreman-Mackey, D., Hogg, D. W., Lang, D., & Goodman, J. 2013, PASP, 125, 306

Fortney, J. J., Lodders, K., Marley, M. S., & Freedman, R. S. 2008, ApJ, 678, 1419

Fortney, J. J., Marley, M. S., & Barnes, J. W. 2007, ApJ, 659, 1661

Fortney, J. J., Mordasini, C., Nettelmann, N., et al. 2013, ApJ, 775, 80

Freedman, R. S., Lustig-Yaeger, J., Fortney, J. J., et al. 2014, ApJS, 214, 25

Frelikh, R., & Murray-Clay, R. A. 2017, ArXiv e-prints, arXiv:1708.00862

Guillot, T. 2010, A&A, 520, A27

Horne, K. 1986, PASP, 98, 609

Kreidberg, L. 2015, PASP, 127, 1161

Kreidberg, L., Bean, J. L., Désert, J.-M., et al. 2014, Nature, 505, 69

Kreidberg, L., Line, M. R., Bean, J. L., et al. 2015, ApJ, 814, 66

Lacis, A. A., & Oinas, V. 1991, J. Geophys. Res., 96, 9027

Line, M. R., Knutson, H., Wolf, A. S., & Yung, Y. L. 2014, ApJ, 783, 70

Line, M. R., Vasisht, G., Chen, P., Angerhausen, D., & Yung, Y. L. 2011, ApJ, 738, 32

Line, M. R., Stevenson, K. B., Bean, J., et al. 2016, AJ, 152, 203

Madhusudhan, N., Amin, M. A., & Kennedy, G. M. 2014, ApJL, 794, L12

Madhusudhan, N., Harrington, J., Stevenson, K. B., et al. 2011, Nature, 469, 64

Mollière, P., van Boekel, R., Dullemond, C., Henning, T., & Mordasini, C. 2015, ApJ, 813, 47

Mordasini, C., van Boekel, R., Mollière, P., Henning, T., & Benneke, B. 2016, ApJ, 832, 41

Morley, C. V., Fortney, J. J., Marley, M. S., et al. 2012, ApJ, 756, 172

—. 2015, ApJ, 815, 110

Morley, C. V., Knutson, H., Line, M., et al. 2017, AJ, 153, 86

Moses, J. I., Madhusudhan, N., Visscher, C., & Freedman, R. S. 2013, ApJ, 763, 25

Močnik, T., Hellier, C., Anderson, D. R., Clark, B. J. M., & Southworth, J. 2017, MNRAS, 469, 1622

Öberg, K. I., Murray-Clay, R., & Bergin, E. A. 2011, ApJL, 743, L16

Pollack, J. B., Hubickyj, O., Bodenheimer, P., et al. 1996, Icarus, 124, 62

Saumon, D., Chabrier, G., & van Horn, H. M. 1995, ApJS, 99, 713

Skemer, A. J., Marley, M. S., Hinz, P. M., et al. 2014, ApJ, 792, 17

Stevenson, K. B., Bean, J. L., Seifahrt, A., et al. 2014, AJ, 147, 161

Thorngren, D. P., Fortney, J. J., Murray-Clay, R. A., & Lopez, E. D. 2016, ApJ, 831, 64

Tinetti, G., Tennyson, J., Griffith, C. A., & Waldmann, I. 2012, Philosophical Transactions of the Royal Society of London Series A, 370, 2749

Zahnle, K. J., & Marley, M. S. 2014, ApJ, 797, 41

Zhou, Y., Apai, D., Lew, B. W. P., & Schneider, G. 2017, AJ, 153, 243